

Full paper

A three-electrode multi-module sensor for accurate bodily-kinesthetic monitoring

Haobin Wang^a, Yu Song^a, Hang Guo^{a,b}, Ji Wan^a, Liming Miao^a, Chen Xu^{a,b}, Zhongyang Ren^c, Xuexian Chen^{a,b}, Haixia Zhang^{a,b,*}

^a National Key Laboratory of Science and Technology on Micro/Nano Fabrication, Institute of Microelectronics, Peking University, Beijing, China

^b Academy for Advanced Interdisciplinary Studies, Peking University, Beijing, China

^c College of Physics and Information Engineering, Fuzhou University, Fuzhou, China



ARTICLE INFO

Keywords:

Three-electrode-sensing
Multi-module
Motion-monitoring

ABSTRACT

In response to the ongoing challenges for health care and human motion monitoring, this work proposes a three-electrode multi-module sensor (TEMS) integrating proximity feedback, compression sensing and stretching perception. With the assist of the porous carbon nanotubes (CNTs)-polydimethylsiloxane (PDMS) patch in optimized parameters, the unification of the device's out-of-plane non-contact sensing and in-plane contact segmental detection is realized. Besides, coordinated with a set of symmetrically patterned Ag nanowires (NWs) electrodes with specified initial conductivity, the device is highly-sensitive to two-dimensional strains and qualified for recognizing the horizontal tension strain as small as 0.077% and the vertical pressure exerted by a piece of scrip (0.18 Pa) in fast response (millisecond level). The anti-interference ability of the signals is ensured by the PDMS encapsulation and regional stiffness of the device. Furthermore, the simplified fabrication process based on PDMS doping/modification is suitable for human skin-attachable applications, especially as the accurate differentiation of similar motions and the time-phased judgment of continuous movements through collaboration among acquisition results.

1. Introduction

With the advent of the smart healthcare electronics, there are growing appeals to highly-sensitive and reliable sensors to accurately visualize various physiological signals [1–3] and movement information [4–7]. Two obvious strategies for high-efficient sensing of body's diverse parameters are as follows: the first is to make a comprehensive record of health indicators by equipping various discrete sensors then synthesizing the acquisitions. For each sensor, the trade-off between high sensitivity and broad sensing range should be considered [8]. Besides, in order to avoid the mechanical damage caused by the dynamic strain and the degradation of performance amid human internal environment, it is required to make a balance between the electrical and mechanical properties (flexibility [9,10], stretchability [11,12], robustness [13], biodegradability [14], etc) of the device. Secondly, a more promising approach is to develop sensors towards multi-functional integration [15–17]. Compared with single-function device, the integrated system should avoid the interference among different parameters [17] and

ensure the overall stability on the premise that the function of each part is guaranteed.

However, both approaches are faced with the challenge of improving the sensing performance of the device itself. Appropriate material selection is critical to maintain the high sensitivity/gauge factor and the linearity of the acquired data. By virtue of the one-dimensional materials, such as metallic nanowires (NWs), carbon nanotubes (CNTs), nanofibers, with inherently high aspect ratio and high-efficiency percolation conductive network, the obtained devices simultaneously exhibit high conductivity and flexibility [18–20]. Structure design is also significant for boosting the sensing behavior: textile-based structure mainly utilizes the change of the overlap area between the top and bottom conductive fibers to feel the strain applied on them [21,22]; Porous structure modifies deformation manner to effectively enhance the sensitivity by subtractive manufacturing technique [23–25]; Hierarchical configuration is superimposed by different micro-nano scale structures to achieve segmental detection at the expense of adding fabrication process complexity [26–28].

* Corresponding author. National Key Laboratory of Science and Technology on Micro/Nano Fabrication, Institute of Microelectronics, Peking University, Beijing, China.

E-mail address: zhang-alice@pku.edu.cn (H. Zhang).

<https://doi.org/10.1016/j.nanoen.2019.104316>

Received 24 September 2019; Received in revised form 8 November 2019; Accepted 19 November 2019

Available online 22 November 2019

2211-2855/© 2019 Elsevier Ltd. All rights reserved.

In addition to passively responding to external stresses through crack propagation [29] or contact resistance variation [30–32], etc, it is necessary to flourish the diversity and integrity of data collection through active (no power excitation required) means based on the triboelectric or piezoelectric effects [33–37]. Thereby, non-contact electrostatics motion recognition is in a period of budding development [38–40]. Moreover, processing technology and the possibility of large-scale production [41–43] are also worth exploring.

Compared with traditional healthcare equipment, wearable/epidermal sensors have marked their presence with real-time field monitoring, better comfort and portability. However, integrated sensing systems are still at embryonic stage since the dimensions and types of signals collected are still limited. Furthermore, the ability to monitor small-scale movements such as small motions of joints and even weak physiological signals needs to be improved.

Here, aiming at improving the richness and accuracy of collected data, we present a multi-functional three-electrode sensor (TEMS) integrates the ability of electrostatic proximity detection and two-dimensional resistive-type strain sensing. The selection of polydimethylsiloxane (PDMS)-nanomaterial composites with specific structural design guarantees the high performance of the device. Porous CNT-PDMS conductive elastomer possesses large surface area and sufficient roughness to perceive loaded pressure as well as provides considerable contact area to form connected paths. Folded-line Ag NWs coated on the PDMS substrate accelerates the crack growth rate by concentrated stress. With the combination of the PDMS encapsulation and regional treatment of matrix-crosslinker ratio of PDMS, the humidity effect on performance can be avoided and the piezoresistive module remains stable when receive tensile stress. The synergy of the above capabilities proves the potential of such TEMS for human applications and paves the way for bodily-kinesthetic monitoring.

2. Results and discussion

2.1. Design and process of the TEMS

The overall design of the TEMS is illustrated in Fig. 1a, which mainly consists of the top and bottom parts. The bottom structure is a pair of patterned Ag NWs electrodes based on the PDMS substrate sensitive to tension, the rules of which are portrayed in Fig. 1b. Above the

interdigital Ag NWs, there is a porous CNT-PDMS patch encapsulated in PDMS for sensing compression. The fact that the ratios of PDMS's base resin to cross-linker in the top and bottom structures are different will be discussed further in Section 2.4. Therefore, the CNT-PDMS patch acts as the conduction bridge, allowing the device to sense two-dimensional strains and convert them into resistance change between the 1st and 2nd Ag NWs electrodes. Furthermore, when a charged object approaches to the device, there will be opposite charges induced on the 3rd CNT-PDMS electrode together with a transient current passing through.

As a consequence, such device possesses three basic modules for skin-attachable applications showed in Fig. 1c. In addition to the easy identification of induced electrical signals from charged object, the trends of resistance response caused by horizontal stretching and vertical compression are exactly opposite, which can help us reversely speculate on what kind of external stimuli exerted. Besides, the equivalent circuit of the device is disclosed in Fig. 1d, intuitively illustrating the physical mechanisms behind the device. R_P is the piezoresistance of CNT-PDMS patch and R_S is the stretching-resistance of Ag NWs. R_C stands for the contact resistance between the top and bottom layers. σ_1 and σ_2 are surface charge densities of the charged object and induced CNT-PDMS patch, respectively.

The relatively versatile and facile process of the TEMS is depicted in Fig. 2 (more details can be found in **Experimental Section**). The top structure process combines the conductive polymer composites with mold-transferring method. Profiting from the excellent conductivity of CNTs and the intrinsic flexibility of PDMS, the obtained patch exhibits both elegant electrical and mechanical properties. Additionally, with the assistance of the laser-engraving polymethyl methacrylate (PMMA) mold and sugar sacrificial templates, the produced porous patch encapsulated by PDMS on the top and side can possess finely controllable shape and deliver higher sensitivity compared to the traditional solid one (which will be confirmed in Section 2.3). As for the process of bottom structure, selecting the laser-patterning polyimide (PI) mask and spray-coating technique, the film thickness and initial resistance of the thin layer of Ag NWs could be accurately controlled. Patterned substrate (in Fig. 2b iii) contributes to concentrated strain during stretching [44].

Subsequently, uncured PDMS is utilized to bond the top and bottom structures together for forming a reliable contact (the initial total resistance of the device is dominated by such contact resistance). The pictures and basic physical properties of assembled sensor are

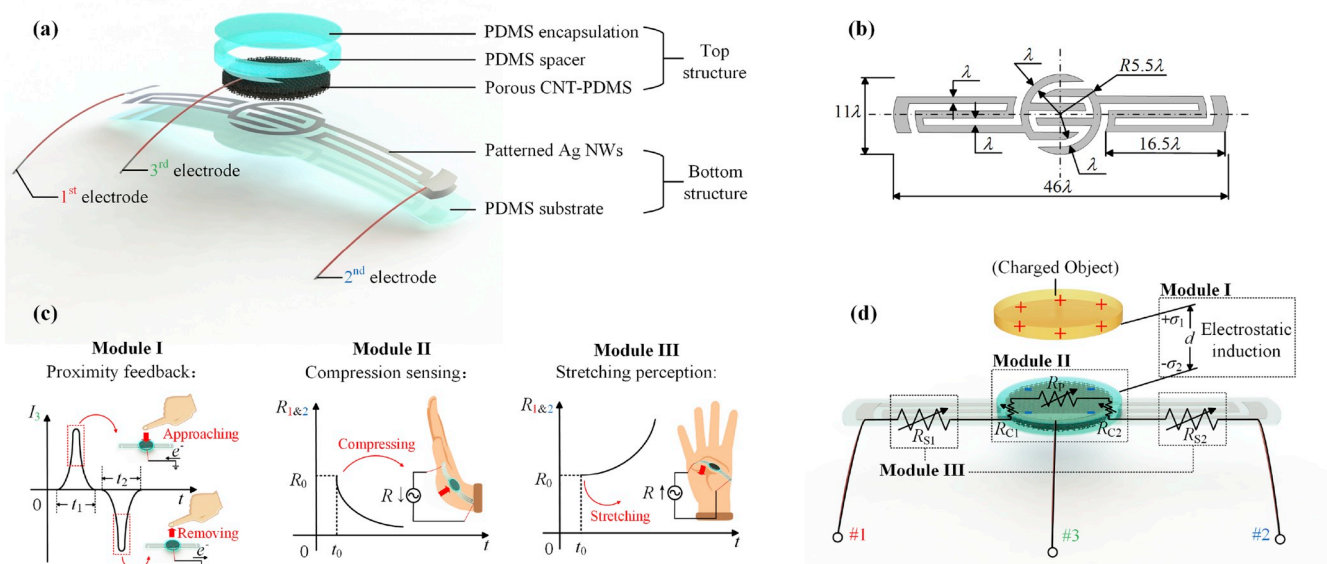


Fig. 1. Design of TEMS with three main functional modules. (a) Structural schematic of the device. (b) Pattern layout of the Ag NWs film (adjust λ meeting actual needs). (c) Distinct signals generated from different body motions by the three modules. (d) Equivalent circuit based on the electrostatic induction and strain-sensitive resistances.

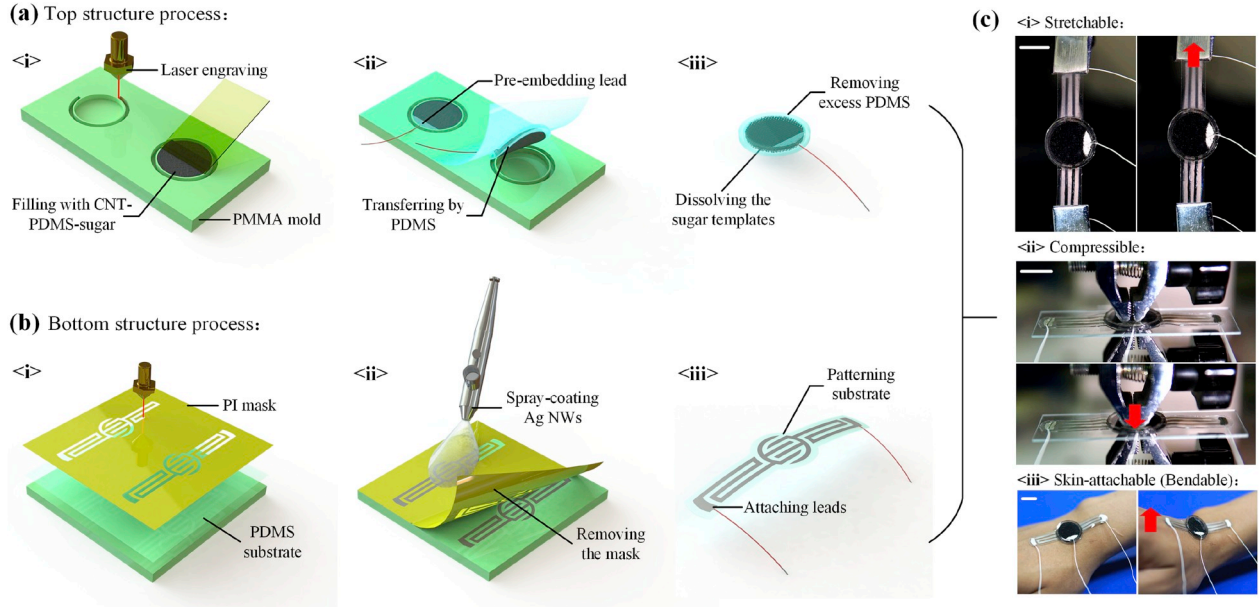


Fig. 2. Fabrication process of TEMS. (a) Fabrication process of top porous CNT-PDMS patch. (b) Fabrication process of bottom patterned Ag NWs electrodes. (c) Optical images of the assembled device and basic physical features (scale bar: 5 mm).

showcased in Fig. 2c. The device exhibits flexibility in two dimensions when tested. Besides, it can be bent when conformably attached to the skin, which is essential for collecting reliable data.

2.2. Performance of the proximity feedback module

The first remarkable module of the device is the proximity feedback of out-of-plane objects. As shown in Fig. 3a, when a charged object (positively, for example) remains quiescent above the device, opposite charges are induced on the patch's upper surface due to the electrostatic induction effect. According to the Gauss's Law, the potential (φ) at the distance r from the charged object is obtained as:

$$\varphi = \frac{q}{4\pi\epsilon_0 r} \quad (1)$$

, where q is the charge amount of the object, ϵ_0 is a proportional constant (see Fig. S1 for details). Such φ can be directly collected and used to reflect the distance from the object. Then normal component of the electric field (E_{n+}) here is:

$$E_{n+} = -\frac{q}{4\pi\epsilon_0} \cdot \frac{1}{r^2} \cdot \frac{d}{r} = -\frac{1}{4\pi\epsilon_0} \cdot \frac{d \cdot q}{(d^2 + x^2)^{3/2}} \quad (2)$$

, where d and x represent the vertical and horizontal components of the r , respectively. Furthermore, adopting the image charge theory (see Fig. S1), the surface charge density (σ) at any point is:

$$\sigma(d, x) = \epsilon_0 \cdot E_{n+}(d, x) = -\frac{2d \cdot q}{4\pi(d^2 + x^2)^{3/2}} \quad (3)$$

That is, the distribution of induced charges is directly related to d , x and q . When the charged object approaches/leaves the device, the amount of the charges induced on the patch will change, causing charge transfer between the patch surface and the reference electrode to balance the potential change.

As a proof of concept, Fig. 3b simulates the change of surface induced potential when the distance between the charged object and the device varies. The actual collected current waveform is shown in Fig. 3c (based on the fabrication process and charged object obtained by triboelectric charging mentioned in Experimental Section, the positive peak of the induced current is 3 nA at 0.5 Hz and the approaching/removing

distance of (0.8, 5.5) cm), from which we could judge the moving tendency of the out-of-plane object through direction of current.

To further confirm the feasibility of our scheme and reveal the factors affecting the induced process, we conducted several control experiments. Firstly, it can be known from the following formula:

$$I(t) = \frac{\partial Q(t)}{\partial t} = \gamma \cdot \frac{\partial \varphi(t)}{\partial t} \quad (4)$$

, where Q stands for the total induced charges and γ is the scale coefficient, that the induced current intensity is related to the change of induced φ per unit time. Combined with Equation (1), the distance of the proximity judgment is treated as an independent variable in Fig. 3d. When the approaching distance is closer, more charges are accumulated in unit time, thereby causing a larger current signal.

Secondly, we can learn from Equation (4) that the current intensity is entwined with the time per induced Q change. Thus we observe the frequency response of the induced signal from 0.5 Hz to 4 Hz in Fig. 3e. The shorter the time taken for a single cycle of charge transfer, the larger the peak-to-peak value of the induced current becomes.

Thirdly, if the closer object is charged negatively (see Fig. 3f), then the polarity of the collected signal is reversed, which is able to distinguish the type of object charged.

Besides, Fig. 3g signifies that such feedback can be repeated when the proximity object is charged stably. In actual situations, the surface charge cumulated by frictional electrification and the corresponding detected current will gradually decay with time (see Fig. 3h).

2.3. Performance of the compression sensing module

Regarding the second major module for compression sensing, this work introduces the porous structure into conductive elastomer. According to the COMSOL mechanical simulation in Fig. 4a, the stresses of the porous experimental group are more concentrated and it is more susceptible to deformation under the same pressure. Both two are boiled down to the slash in the Young's modulus caused by the porous effect, which can be explained by the following equations (more details in Fig. S2):

$$\frac{E_1^*}{E_s} = \left(\frac{l}{h}\right)^3 \frac{\cos \theta}{(h/l + \sin \theta) \sin^2 \theta} \quad (5)$$

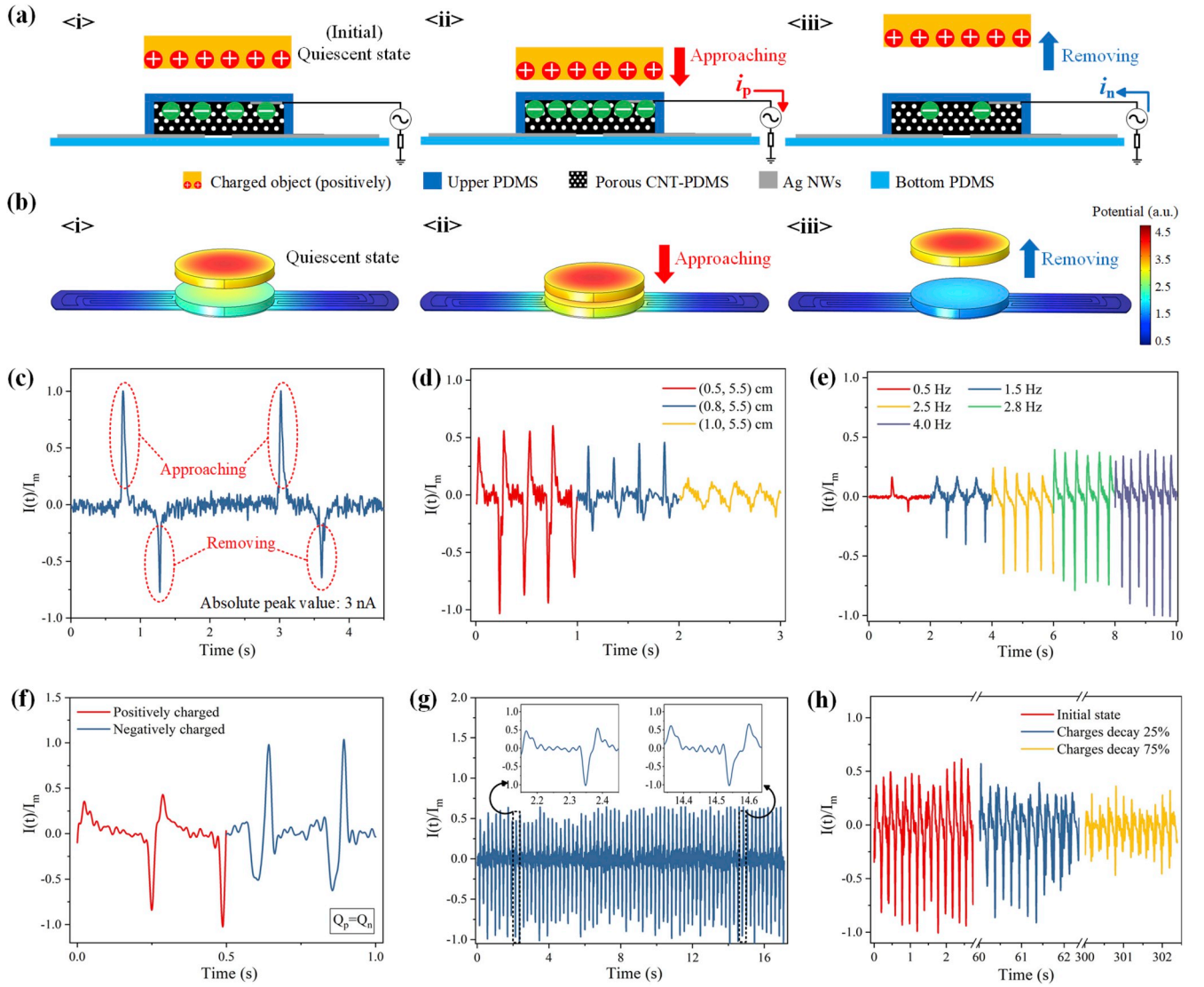


Fig. 3. Performance of the module I, proximity feedback. (a) Schematic illustration of the proximity signal generation process. (b) Corresponding COMSOL electrostatic simulation of the three states. (c) Collected current waveforms when charged object approaching/removing from the device (I_m represents the peak value of the signals on the order of nA, the same below). (d) Relationship between induced current and approaching/removing distance. (e) Frequency response of induced current. (f) Induced signals of the objects with opposite polarity. (g) Cycling reliability of sensing performance. (h) Relationship between induced current intensity and charge amount of the object.

$$\frac{E_2^*}{E_s} = \left(\frac{t}{l}\right)^3 \frac{h/l + \sin \theta}{\cos^3 \theta} \quad (6)$$

, where t , l , h and θ represent the parameters of the pore wall of the structure (see Fig. S2a); E_1^* and E_2^* are the equivalent Young's modulus in horizontal and vertical dimensions, respectively; E_s is the Young's modulus of the solid material. In particular, for a regular hexagon having a uniform thickness of pore walls:

$$\frac{E_1^*}{E_s} = \frac{E_2^*}{E_s} = 2.3 \left(\frac{t}{l}\right)^3 \quad (7)$$

Here, t is much smaller than l , so the porous structure behaves much softer than the solid one. If only the characteristics of the structure itself are considered, the sensitivity of the piezoresistive patch can be described as:

$$S = \frac{dR/R}{dP} = \frac{1}{\rho} \frac{\delta \rho}{\delta P} + \frac{1}{E} + \frac{2\nu}{E} \frac{1}{E} \quad (8)$$

, where S , P , ρ and ν stand for the sensitivity, applied pressure, resistivity, Poisson's ratio of the patch. From Equations (7) and (8), we can conclude that the higher the porosity results in a smaller E , and the higher S of the device. However, taking into account the stretch-sensing performance of the device, E is not as small as possible, which will be explained further below.

Fig. 4b are the SEM images at different scales. On the one hand, pores of about 50 μm confirm the feasibility of the fabrication process. On the other hand, the intertwined CNTs exposed on the surface ensure the electrical conductivity and sensing properties of the structure.

The resistance-pressure curve during the compressing-releasing cycles is shown in Fig. 4c, which reflects the extremely high sensitivity at low applied pressure (with initial resistance of approximately 75 k Ω). The complete detection range and interpretation for segmented sensitivities are revealed in Fig. S3 and Table S1 (changes of the contact resistance, pore resistance and resistance of the material itself are successively dominant as the pressure increasing). Besides, signal hysteresis almost does not exist.

Ignoring the internal resistance of the test equipment, the change in

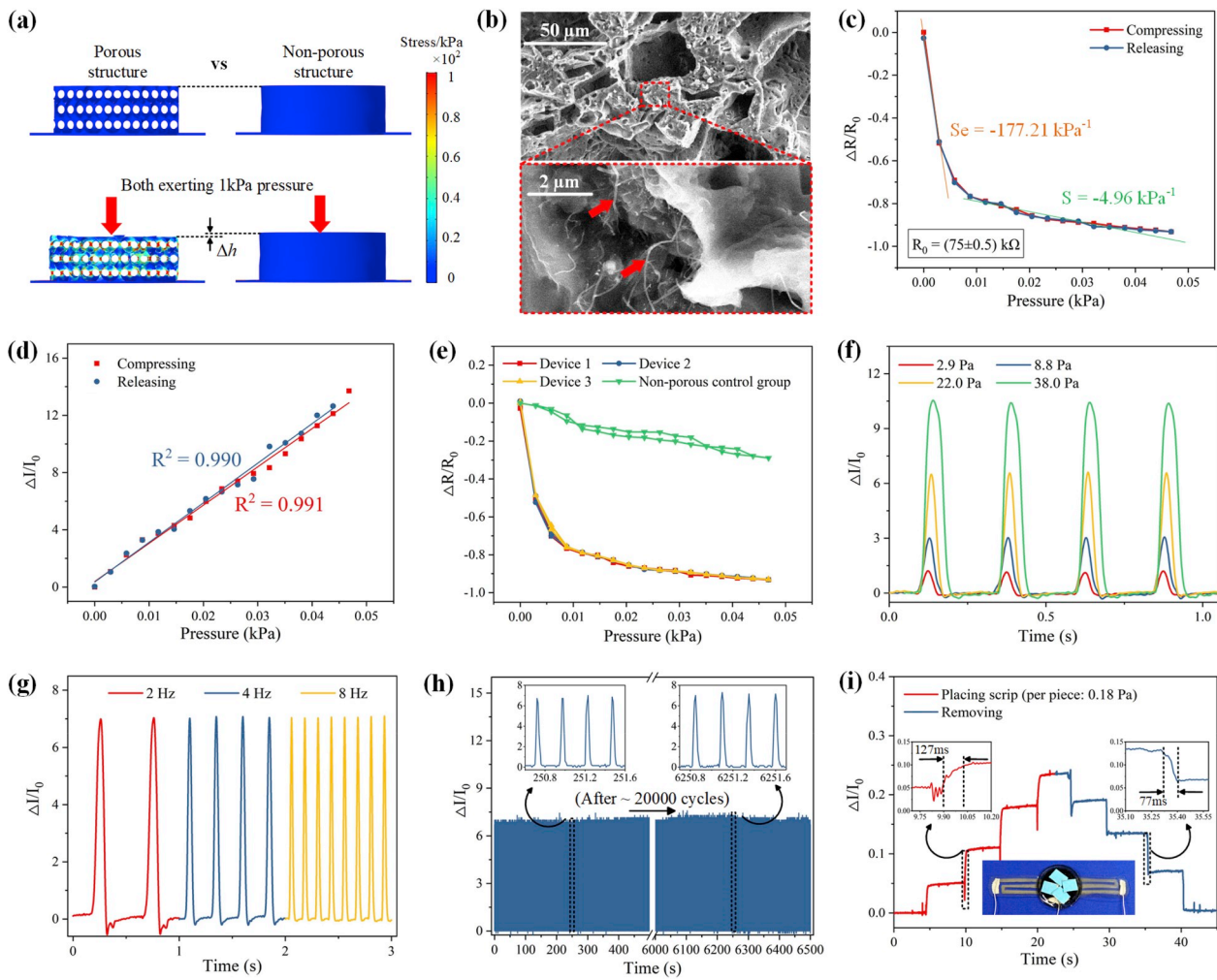


Fig. 4. Performance of the module II, compression sensing. (a) COMSOL mechanical simulation of porous CNT-PDMS structure versus non-porous structure. (b) SEM photographs of porous structure (the uncovered CNTs are marked with red arrows). (c) Relationship between resistance response and applied pressure during the compressing-releasing cycle. (d) Current-pressure curve showing a quasi-linear relation, with deviation from linear fit better than $R^2 = 0.99$ (R^2 : coefficient of determination). (e) Performance uniformity between devices, as well as the comparison with non-porous structure. (f) Current response under different applied pressures. (g) Current response at different compressing frequencies. (h) Cycling tests and stability of the current response. (i) Pressure detection limit (the middle inset shows the measuring method) and response time (the upper inset pictures show the enlarged view of marked places) of the device.

current corresponding to the resistance change of the device is:

$$\frac{\Delta I}{I_0} = \frac{I(t) - I_0}{I_0} = \frac{\frac{V}{R(t)} - \frac{V}{R_0}}{\frac{V}{R_0}} = \frac{R_0 - R(t)}{R(t)} = -\frac{\Delta R}{R(t) - R_0 + R_0} = -\frac{\frac{\Delta R}{R_0}}{\frac{\Delta R}{R_0} + 1} \quad (9)$$

, where I_0 , $I(t)$ and ΔI refer to the initial value, real-time value and change amount of the current, the same to the resistance R ; V is the applied test voltage. Thus, the transformed current-pressure curve is portrayed in Fig. 4d, showing a quasi-linear relation ($R^2 > 0.99$), which is extremely advantageous to the back-end processing circuit.

For the purpose of maximizing the performance of the device, we compared several key parameters of the porous CNT-PDMS patch in Fig. S4. It is worth noting that each parameter will both affect the compressing and stretching sensing of the device (stretch-sensing will be demonstrated in Section 2.4). Therefore, weighing the coupling impacts on the performances and the feasibility of the process, we have made clear that the pore diameter, CNTs content and thickness of the porous CNT-PDMS patch are $50 \mu\text{m}$, 7 wt% and 2 mm, respectively.

Based on the above process parameters, a batch of devices were fabricated and evaluated for performance uniformity in Fig. 4e. From the resistance response curve, it is intuitive that the difference between the three different devices is tiny. Besides, the sensitivity of the non-

porous control group is indeed far less than that of the porous structures.

According to Fig. 4f, the current through the device can respond repeatedly to the different applied pressures. Since the pressure is applied by periodic oscillations of Modal Shaker, the response current signal is a quasi-sine wave with different pulse widths, from which the high responsivity of the device can be seen. Besides, we also studied the current response of the device at different compressing frequencies as showed in Fig. 4g, where the response current of the device is still regular and distinguishable even at 8 Hz.

Fig. 4h illustrates the excellent sensing stability of the device during the cyclic tests. The insets show the amplitude of the current change is basically the same before and after repeated tests. The major ten-micron pores of the structure maintain their original shapes after cyclic compressions and the CNT network that is still intertwined can be used as evidences in Fig. S5. It is worth mentioning that the PDMS package can protect the porous patch and the embedding lead free from moisture intrusion [45] on the one hand, which has been demonstrated in Fig. S6 by a control experiment (Otherwise, moisture entering the pores will cause a non-negligible drop in the structural resistance); On the other hand, the sidewall package acts as a spacer to make the upper and lower layers form effective contact and ensure the initial contact resistance stable during mechanical deformation.

We also characterized the minimum detection limit and response time. In order to quantify and refine the applied pressure, we selected scrip as the “weight”. It can be seen from Fig. 4i that the current exhibits a resolvable step change when the pieces of scrip (each piece: 0.18 Pa) are placed/removed one by one. In this case, the rise and fall times of the signal are 127 ms and 77 ms, respectively.

2.4. Performance of the stretching perception module

The third inherent module of the device is the perception of stretching. Ag NWs film is easily prepared by spray-coating, and its gauge factor is further amplified by structural design. Fig. 5a is the COMSOL simulation of the stress distribution during stretching. The rationale behind the design is revealed in Fig. S7a. In addition to being able to concentrate stress to initiate crack propagation, the change in resistance of the folded-line structure is superimposed due to the series effect.

The phenomenon that the middle piezoresistive patch remain stable during stretching is proved theoretically in Fig. S8, mainly attributed to two reasons: firstly, the thickness of the middle patch is much larger than that of the two sides; secondly, the ratio of the PDMS's base resin to

cross-linker used in middle structure is relatively smaller, leading to a more complete cross-linking reaction. These two make the stiffness (k) of the middle patch much larger:

$$E_2 t_2 \gg E_1 t_1, E_3 t_3 \quad (k \propto Et) \quad (10)$$

, where E_2, t_2 represent the Young's modulus and thickness of middle patch, respectively; E_1, t_1 and E_3, t_3 are the ones of the both easy-to-stretch sides. According to structural symmetry, consider $E_1 \cong E_3, t_1 \cong t_3$, the strain of the entire structure ϵ_{entire} can be expressed as:

$$\epsilon_{entire} = \frac{E_2 t_2 \epsilon_2}{E_1 t_1} \frac{l_1 + l_3}{l_1 + l_2 + l_3} + \epsilon_2 \frac{l_2}{l_1 + l_2 + l_3} \quad (11)$$

, where ϵ_2, l_2 are the strain and the diameter of the middle patch, respectively, l_1 and l_3 are the original lengths of the both sides. The first term of Equation (11) is the proportion of the strain on both sides in the whole, and the second is the middle's. Therefore, the greater the difference between $E_1 t_1$ and $E_2 t_2$, the smaller the relative deformation of the middle patch.

The advantages of stabilizing the middle structure are as follows: firstly, if the middle patch is obviously stretched, then the top and

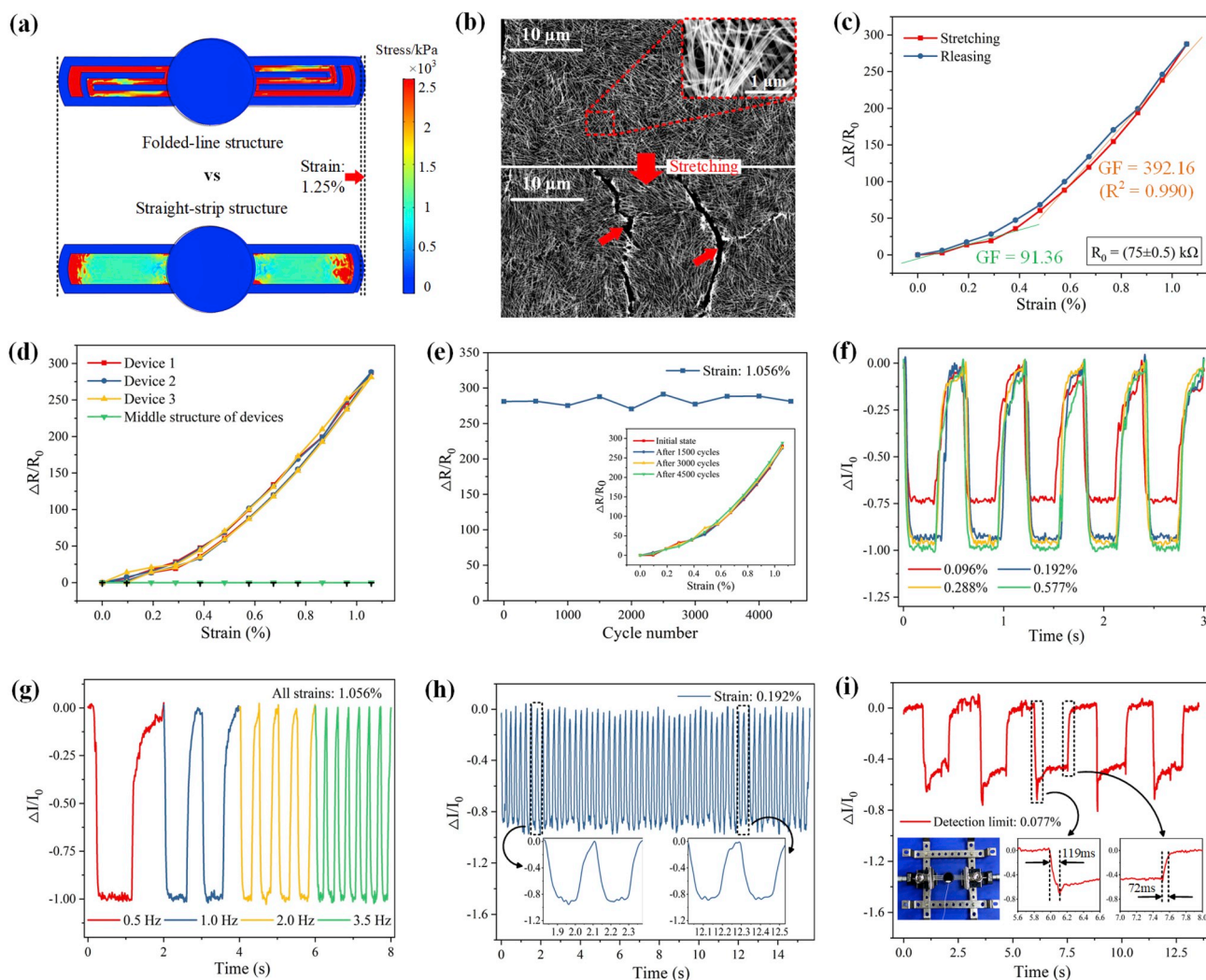


Fig. 5. Performance of the module III, stretching perception. (a) Mechanical simulation of folded-line Ag NWs structure versus straight-strip structure using COMSOL software. (b) SEM photographs of Ag NWs thin layer before and after stretching (red arrows mark the crack propagation). (c) Relationship between resistance response and applied strain during the stretching-releasing cycle. (d) Performance fluctuation between devices, as well as the stable resistance of the middle piezoresistive patch during stretching. (e) Performance retention of the device during 4500 tensile tests (inset shows the negligible deviations of the resistance-strain curves). (f) Current response under different applied strains. (g) Current response at different stretching frequencies. (h) Stability test of the current response. (i) Strain detection limit (the left inset shows the test platform) and response time (inset images on right side).

bottom layers are simultaneously compressed, which will introduce a coupling resistance effect; secondly, avoid the deterioration of the upper and lower contact even warpage during the multiple stretching process; thirdly, similar to the traditional island-bridge structure (using serpentine interconnected “bridge” to disperse the applied strain while the active devices on the “island” with stronger structural strength remain relatively stationary) [15,46,47], such design can protect the functional units integrated thereon from stress damage.

Fig. 5b shows the SEM images of Ag NWs thin layer before and after stretching, where the tightly interlocking Ag NWs ensure high

conductivity of the film formation, and the occurrence of the crack propagation is a good explanation for its resistance surge after stretching (after releasing, the formed cracks cannot completely recover, but the resistance is barely increased).

The relationship between resistance response and applied strain (at the strain rate of 0.096%/s) is reflected in Fig. 5c. Similar to the above piezoresistive sensitivity, the gauge factor of stretching is also segmented: at low strain (<0.4%), the gauge factor is around 91.36; when the strain is greater than 0.4%, the gauge factor becomes higher (GF = 392.16) and the curve becomes quasi-linear ($R^2 = 0.99$). Here, in

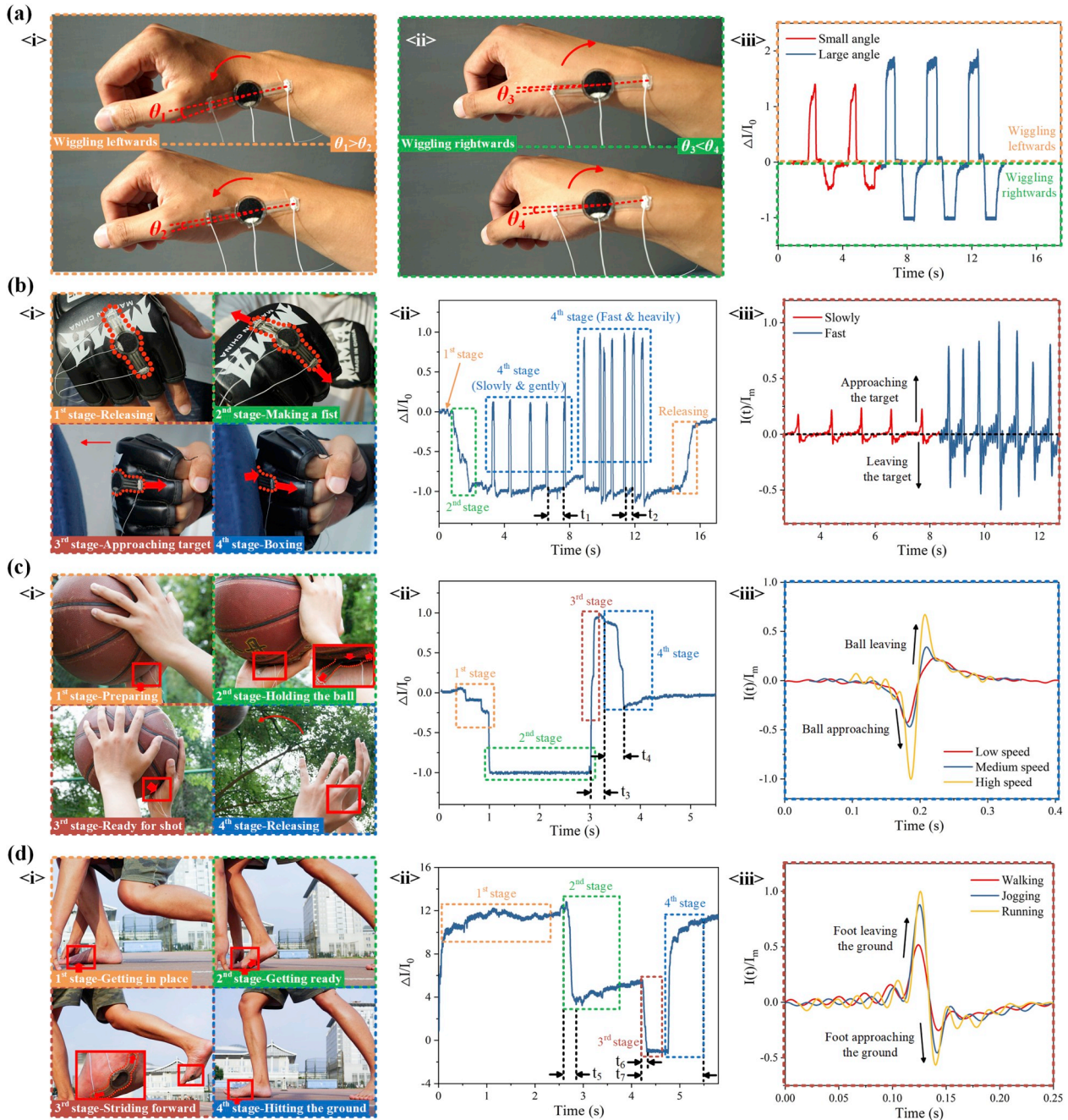


Fig. 6. Examples of the TEMS for bodily-kinesthetic detection (with dotted lines in different colors indicating different phases of actions and corresponding signals). (a) Precise distinction of similar movements: schematics of wrist wiggled left <i> and right <ii> at different angles; <iii> Corresponding detection current waveform between the 1st & 2nd electrodes. (b)–(d) Time-phased judgments of continuous combined motions: <i> Step-by-step diagram of the entire set of actions (with red dashed outlining the attachment location of the device, thick arrows marking the direction of force applied, and thin arrows marking the trend of action); <ii> Detection current signal between the 1st & 2nd electrodes corresponding to different action phases (with labeled characteristic time); <iii> Corresponding current signal detected by the 3rd electrode of (b) Boxing training, (c) Basketball shooting and (d) Squat starting. (The device attachment locations of the (c) and (d) have been further visually displayed in Fig. S12).

order to pursue a better gauge factor, we sacrifice the detection range to some extent (maximum conductive strain: 1.056%). Similar to module II, we have changed the ordinate of this curve to $\Delta I/I_0$ with linearity degraded, and given corresponding explanations in Fig. S9.

Furthermore, we compare the stretch-sensing properties under different spray-coating thicknesses in Fig. S7b. The larger the initial resistance of Ag NWs film results in a larger gauge factor, while its stretchability decreases. The performance uniformity between the same batch of devices can be obtained from Fig. 5d. Besides, the resistance change of the middle patch is indeed ignorable during tests.

Fig. 5e, the performance retention during 4500 tests, demonstrates that the resistance increases under multiple ultimate stretching maintains about 280 times of the initial value. Combined with the inset image, we can conclude that the device exhibits the excellent damage tolerance for potential repeated and reversible usage.

The current responses to applied strains with different degrees and different frequencies are clearly depicted in Fig. 5f and g, respectively. Its stable and reliable response paves the way for the applications in human motion detection and health management. We have also explored the signal fluctuation under the cyclic applied/removed strain (see Fig. 5h), which can further prove the durability of the device.

With the help of an optical micro-displacement platform, the periodic strain applied can be precisely controlled. As shown in Fig. 5i, when the unit strain is as small as 0.077%, the device can still respond in a timely and accurate manner, and the fall and rise times of the signal are 119 ms and 72 ms, respectively.

When there are multiaxial strains, or the strain does not follow the tensile direction of the device, it is necessary to enrich the device's tensile dimension. Fig. S10 describes a way to acquire richer information through biaxial stretching design.

2.5. Demonstration of TEMS for bodily-kinesthetic monitoring

As can be seen from the above description, the whole process is based on the laminated conductive composite material obtained from the PDMS matrix, which is suitable for skin-attached applications.

On the one hand, the high sensitivity/gauge factor of the device are very beneficial for the precise differentiation of the similar movements. As the example given in Fig. 6a, attaching the device to one side of the wrist joint can effectively distinguish its left or right twist. When the wrist is wiggled to the left, the middle patch is squeezed, leading the resistance significantly reduced (The resistance change of the Ag NWs folded lines on both sides can be neglected. See Fig. S11 for details), and the amplitude of wiggling can be read from the increased amplitude of the current (in Fig. 6a iii). When the wrist is turned oppositely, the Ag NWs on both sides are stretched. At this time, the resistance change caused by stretching is dominant, so that the current signal is detected in opposite directions.

On the other hand, the cooperation between the three modules can achieve the purpose of real-time monitoring the continuous movements. Detailedly, the proximity feedback module is mainly responsible for the movement trend of the human body before contacting with surrounding environment and the in-plane stress measurement after contact is handled by the other two modules. It is considered that the friction electrification and charge degradation between the interface of the contact objects are approximately dynamic equilibrium under selected scenarios of continuous movements and the minimum distance during non-contact approaching is infinitely zero. At this time, the variable that mainly affects the magnitude of the induced current is the speed (frequency) of approaching/removing process.

For one thing, supervising the speed, frequency and strength of boxing is critical to improving the quality of training. At the first stage of Fig. 6b, the device, attached to the metacarpophalangeal joint, is free from external forces and the resistance remains stable. Entering the second stage with the hand clenched, the stretched Ag NWs lines induce the resistance getting larger. Then, in the process of approaching the

target, the transient induced current is detected (when the glove is frictionally charged). As disclosed in Fig. 6b iii, the magnitude and polarity of the current can reflect the speed and direction of the boxing, respectively. In the fourth stage, the glove is in contact with the target, and the device is superimposed with a compressive strain, so that the resistance drops. Moreover, the magnitude and frequency of the resistance reduction can reflect the strength and frequency of boxing (t_1 and t_2 in Fig. 6b ii correspond to two different punch modes).

For another application, correcting the shooting action is one of the effective ways to facilitate the shooting rate. As depicted in Fig. 6c, at the stage of catching and preparing the ball, the device is subjected to a subtle tension due to the small bending of the wrist. Then the player holds the ball aiming at the basket, his opisthenar and forearm are nearly vertical and the tension of the device (attached to the thenar eminence) is cumulative. Meanwhile the ball has compressive stress on the device (this moment, the stretching is dominant, so the whole resistance increases). When the shot is ready, the tension mitigates, and sufficient squeezing between the interface facilitates a larger initial velocity of the ball, resulting in a significantly resistance drop. In the final stage, the ball is off the hand to make the resistance restore, and the charge on the ball surface can reflect the speed of the releasing process (see Fig. 6c iii). Besides, the t_3 and t_4 in Fig. 6c ii could represent the time of power-accumulating and throwing, respectively.

Meanwhile, we also attached the device to the first metatarsophalangeal joint of the forefoot monitoring the typical stages of the squat start. Initially, when the athlete gets in place, the device is exposed to significant compressive stress between the forefoot and the ground, showing a much smaller resistance. Immediately afterwards, the athlete squats and shifts his center of gravity to get ready for start. At this time, the stretching of the device caused by the joint bending makes the superimposed resistance enhance, which is depicted in Fig. 6d ii with t_5 on behalf of the preparatory reaction time. The third and fourth stages are the athlete's lifting foot start and the foot landing, which are subjected to obvious stretching and obvious squeezing respectively. Real-time current changes are recorded with t_6 representing the start-up response time and t_7 reflecting the starting step frequency. In addition, as can be seen from Fig. 6d iii, the speed of the foot leaving and approaching the ground can be reflected by the amplitude of induced current between the device and the ground (charged when the foot hits it).

For the electrostatic induction signal and the mechanical sensing signal in each application scenario, simultaneous acquisition can be performed through two paths (1st electrode to 2nd electrode & 3rd electrode to ground), which is further illustrated in Fig. S13. Since the electrostatic induction module is equivalent to a single-electrode triboelectric nanogenerator, for later wireless applications, a metal pad can be selected as the reference electrode. The signal of the mechanical sensing modules can be wirelessly read out using RFID technology and avoid the use of the battery [48].

Furthermore, multiple devices can be attached to different parts of the body and cooperated to record systemic motion information stably and accurately, then may match the data processing and machine learning algorithms to fit the optimal parameters for novice training.

3. Conclusion

Herein, based on three integrated detection modules described above, we demonstrate the device's capability of individually achieving proximity feedback, compression sensing and stretching perception. Firstly, the design of porous CNT-PDMS patch connecting two patterned Ag NWs electrodes with optimal parameters is the main reason behind the high-achieving sensitivity/gauge factor and detection limits (strain: 0.077%, pressure: 0.18 Pa). Secondly, the strategies of encapsulation and non-uniform stiffness enhance the signals' insensitivity to interferences and lay the foundation to the stable and reliable responses of external stimuli. Thirdly, with the in-plane and out-of-plane as well as

the multi-dimensional sensing approaches, the device is promising for accurately distinguishing similar actions and real-time identifying movements, which satisfies the trends of fast-growing smart healthcare.

4. Experimental section

4.1. Fabrication of porous CNT-PDMS elastomer

The CNT-PDMS elastomer itself is prepared by solution- volatilization. Besides, we impart the porous structure to the elastomer with the aid of sugar sacrificial templates. The elastomer can be shaped by PMMA mold using laser machining (VolleRun Laser Technology Co., Ltd.). Toluene is selected (as cosolvent) to add into the mixture of multi-walled CNTs (diameter: 10–20 nm, length: 10–30 μm , purity > 98%, Boyu, Co.) and PDMS base resin (Sylgard 184, Dow Corning Co., USA) at the volume ratio of 5:1, as well as magnetic stirring the mixture for 4 h at room temperature. In order to render the CNTs disperse more homogeneously, the ratio of adding toluene can be slightly adjusted according to the mass fraction of the CNTs (the critical conduction ratio is: 2.5 wt%) in mixture. Until CNTs are mixed into PDMS matrix thoroughly, adding sugar powder with the mass ratio to the matrix of 4:1 and the PDMS cross-linker of 1:10, the total mixture continues to magnetically stirred to evaporate residual toluene. Various sizes of sugar powders are obtained by controlling the time of grinding. Then the mixture is filled into the prepared PMMA mold and baked on the hot plate at 75 $^{\circ}\text{C}$ for 12 h. After the curing process, the sugar templates are dissolved completely by soaking the mixture in an ultrasonic cleaner at 40 $^{\circ}\text{C}$ before drying in air.

4.2. Fabrication of patterned Ag NWs-PDMS thin film

The patterned Ag NWs thin layer formed on PDMS substrate is processed by mask-spraying. We select laser patterned PI as mask which has better interface contact with PDMS than other materials (such as paper, PMMA and nylon) during the spraying process. The details are as follows: firstly, the PDMS base resin and the cross-linker are mixed thoroughly at a mass ratio of 20:1 (the larger the ratio, the smaller the Young's modulus of the prepared PDMS film) and vacuumized for 30 min. The mixture is dropped on the smooth glass surface, followed by spin-coated at 1000 rpm for 60 s (PDMS thickness: ~ 250 μm) and then heated on the hot plate at 80 $^{\circ}\text{C}$ for 60 min to solidify. After placing the designed PI mask onto the surface of PDMS film, oxygen plasma treatment is carried out to make the exposed area hydrophilic by Corona (Electro-Technic Products Inc., USA). Spray-coating ethanol solution of Ag NWs repeatedly using a linear motor to ensure uniform movement of the nozzle until the resistivity of Ag NWs layer reaches the demand. The forming membrane is annealed at 100 $^{\circ}\text{C}$ for 10 min to enhance its conductivity and stability. After removing the PI mask, the patterned Ag NWs-PDMS film is finally gained by carefully peeling off from the glass.

4.3. Fabrication of assembled TEMS

By introducing an outer ring groove into the PMMA mold (see Fig. 2a i) and transferring the CNT-PDMS patch with the PDMS thin film (see Fig. 2a ii), the porous CNT-PDMS patch obtained after dissolving the sugar is exactly encapsulated by PDMS (the ratio of base resin to cross-linker is 10:1) on the top and side. There is a trick that the CNT-PDMS patch should be previously placed in an ultrasonic cleaner together with the mold to dissolve part of sugar. When the patch is softened, it is transferred from the mold for further complete sugar dissolution, in order to improve the integrity of the transfer process and the flatness of the patch bottom, which is the key to guarantee reliable and repeatable contact with Ag NWs. After aligning the upper and lower structures, bond the two together with uncured PDMS (the ratio selected as 20:1) and dry the whole on the hot plate at 75 $^{\circ}\text{C}$ for 4 h. The PDMS adhesive is applied to the bottom of the PDMS spacer and prevented it from

penetrating into the CNT-PDMS patch's bottom as an insulating layer. Furthermore, adopting the pre-embedded lead strategy can effectively improve the bonding strength.

4.4. Characterization and measurement

Morphologies of the porous CNT-PDMS elastomer and Ag NWs-PDMS thin film are observed using Scanning electron microscopy (SEM, Quanta 600F, FEI Co.) with an operation voltage of 5 kV. Resistance response of the TEMS are carried out utilizing a push-pull gauge (Handpi Co.) and using a multimeter to detect real-time changes in resistance. Besides, the ultimate detection pressure of the device is quantitatively controlled using scrips, and its limit detection strain is applied by an optical micro-displacement platform (Misi Automation Co., Ltd.). For the current response, the signals to external stimuli are amplified by a SR570 low-noise current preamplifier from Stanford Research Systems and measured via a digital oscilloscope (Agilent DSO-X 2014A). The periodically controllable pressure can be applied through the Modal Shaker (Sinocera Piezotronics, Inc.) and the periodic strain can be accurately applied by the 2H Microstep driver (TOPCNC Automation Technology Co., Ltd.). Especially in the proximity feedback module (in Section 2.2), the charged object is selected as the positively charged Cu and negatively charged polytetrafluoroethylene (PTFE) films after 30 times of mutual friction (the charge amount is close to that of human frictional charging in daily life).

Declaration of competing interest

The authors declare that they have no known competing financial interests or personal relationships that could have appeared to influence the work reported in this paper.

Acknowledgements

This work was supported by National Key R&D Project from Minister of Science and Technology, China (2016YFA0202701, 2018YFA0108100) and the National Natural Science Foundation of China (Grant No. 61674004).

Appendix A. Supplementary data

Supplementary data to this article can be found online at <https://doi.org/10.1016/j.nanoen.2019.104316>.

References

- [1] S. Lee, A. Reuveny, J. Reeder, S. Lee, H. Jin, Q. Liu, T. Yokota, T. Sekitani, T. Isoyama, Y. Abe, Z. Suo, T. Someya, Nat. Nanotechnol. 11 (2016) 472.
- [2] X. Fan, Y. Huang, X. Ding, N. Luo, C. Li, N. Zhao, S.-C. Chen, Adv. Funct. Mater. 28 (2018) 1805045.
- [3] Z. Lou, S. Chen, L. Wang, K. Jiang, G. Shen, Nano Energy 23 (2016) 7.
- [4] Y. Gao, H. Ota, E.W. Schaler, K. Chen, A. Zhao, W. Gao, H.M. Fahad, Y. Leng, A. Zheng, F. Xiong, C. Zhang, L.-C. Tai, P. Zhao, R.S. Fearing, A. Javey, Adv. Mater. 29 (2017) 1701985.
- [5] C. Wang, X. Li, E. Gao, M. Jian, K. Xia, Q. Wang, Z. Xu, T. Ren, Y. Zhang, Adv. Mater. 28 (2016) 6640.
- [6] Z. Su, H. Chen, Y. Song, X. Cheng, X. Chen, H. Guo, L. Miao, H. Zhang, Small 13 (2017) 1702108.
- [7] Y. Song, H. Wang, X. Cheng, G. Li, X. Chen, H. Chen, L. Miao, X. Zhang, H. Zhang, Nano Energy 55 (2019) 29.
- [8] J. He, P. Xiao, W. Lu, J. Shi, L. Zhang, Y. Liang, C. Pan, S.-W. Kuo, T. Chen, Nano Energy 59 (2019) 422.
- [9] X. Zhang, M. Han, B. Kim, J.-F. Bao, J. Brugger, H. Zhang, Nano Energy 47 (2018) 410.
- [10] X. Chen, Y. Song, Z. Su, H. Chen, X. Cheng, J. Zhang, M. Han, H. Zhang, Nano Energy 38 (2017) 43.
- [11] C. Yan, J. Wang, W. Kang, M. Cui, X. Wang, C.Y. Foo, K.J. Chee, P.S. Lee, Adv. Mater. 26 (2014) 2022.
- [12] X. Chen, Y. Song, H. Chen, J. Zhang, H. Zhang, J. Mater. Chem. A 5 (2017) 12361.
- [13] P. Wei, X. Yang, Z. Cao, X.-L. Guo, H. Jiang, Y. Chen, M. Morikado, X. Qiu, D. Yu, Adv. Mater. Technol. (2019) 1900315.

- [14] C.M. Boutry, Y. Kaizawa, B.C. Schroeder, A. Chortos, A. Legrand, Z. Wang, J. Chang, P. Fox, Z. Bao, *Nat. Electron.* 1 (2018) 314.
- [15] J. Kim, M. Lee, H.J. Shim, R. Ghaffari, H.R. Cho, D. Son, Y.H. Jung, M. Soh, C. Choi, S. Jung, K. Chu, D. Jeon, S.-T. Lee, J.H. Kim, S.H. Choi, T. Hyeon, D.-H. Kim, *Nat. Commun.* 5 (2014) 5747.
- [16] S.Y. Kim, S. Park, H.W. Park, D.H. Park, Y. Jeong, D.H. Kim, *Adv. Mater.* 27 (2015) 4178.
- [17] G. Bae, J.T. Han, G. Lee, S. Lee, S.W. Kim, S. Park, J. Kwon, S. Jung, K. Cho, *Adv. Mater.* 30 (2018) 1803388.
- [18] M. Jian, K. Xia, Q. Wang, Z. Yin, H. Wang, C. Wang, H. Xie, M. Zhang, Y. Zhang, *Adv. Funct. Mater.* 27 (2017) 1606066.
- [19] N. Luo, W. Dai, C. Li, Z. Zhou, L. Lu, C.C.Y. Poon, S.-C. Chen, Y. Zhang, N. Zhao, *Adv. Funct. Mater.* 26 (2016) 1178.
- [20] Y.-C. Lai, B.-W. Ye, C.-F. Lu, C.-T. Chen, M.-H. Jao, W.-F. Su, W.-Y. Hung, T.-Y. Lin, Y.-F. Chen, *Adv. Funct. Mater.* 26 (2016) 1286.
- [21] J. Lee, H. Kwon, J. Seo, S. Shin, J.H. Koo, C. Pang, S. Son, J.H. Kim, Y.H. Jang, D. E. Kim, T. Lee, *Adv. Mater.* 27 (2015) 2433.
- [22] J. Ge, L. Su, F.-R. Zhang, Y. Zhang, L.-A. Shi, H.-Y. Zhao, H.-W. Zhu, H.-L. Jiang, S.-H. Yu, *Adv. Mater.* 28 (2016) 722.
- [23] H. Chen, Y. Song, H. Guo, L. Miao, X. Chen, Z. Su, H. Zhang, *Nano Energy* 51 (2018) 496.
- [24] Y. Song, H. Chen, X. Chen, H. Wu, H. Guo, X. Cheng, B. Meng, H. Zhang, *Nano Energy* 53 (2018) 189.
- [25] Y. Song, H. Chen, Z. Su, X. Chen, L. Miao, J. Zhang, X. Cheng, H. Zhang, *Small* 13 (2017) 1702091.
- [26] J. Mu, C. Hou, G. Wang, X. Wang, Q. Zhang, Y. Li, H. Wang, M. Zhu, *Adv. Mater.* 28 (2016) 9491.
- [27] G.Y. Bae, S.W. Pak, D. Kim, G. Lee, D.H. Kim, Y. Chung, K. Cho, *Adv. Mater.* 28 (2016) 5300.
- [28] Q.-J. Sun, X.-H. Zhao, Y. Zhou, C.-C. Yeung, W. Wu, S. Venkatesh, Z.-X. Xu, J. J. Wylie, W.-J. Li, V.A.L. Roy, *Adv. Funct. Mater.* 29 (2019) 1808829.
- [29] D. Kang, P.V. Pikhitsa, Y.W. Choi, C. Lee, S.S. Shin, L. Piao, B. Park, K.-Y. Suh, T.-i. Kim, M. Choi, *Nature* 516 (2014) 222.
- [30] M. Liu, X. Pu, C. Jiang, T. Liu, X. Huang, L. Chen, C. Du, J. Sun, W. Hu, Z.L. Wang, *Adv. Mater.* 29 (2017) 1703700.
- [31] S. Han, C. Liu, Z. Huang, J. Zheng, H. Xu, S. Chu, J. Wu, C. Liu, *Adv. Mater. Technol.* 4 (2019) 1800640.
- [32] Z. Wang, X. Guan, H. Huang, H. Wang, W. Lin, Z. Peng, *Adv. Funct. Mater.* 29 (2019) 1807569.
- [33] X. Chen, Y. Song, Z. Su, H. Chen, X. Cheng, J. Zhang, M. Han, H. Zhang, *Nano Energy* 38 (2017) 43.
- [34] X. Wang, H. Zhang, L. Dong, X. Han, W. Du, J. Zhai, C. Pan, Z.L. Wang, *Adv. Mater.* 28 (2016) 2896.
- [35] X. Chen, H. Guo, H. Wu, H. Chen, Y. Song, Z. Su, H. Zhang, *Nano Energy* 49 (2018) 51.
- [36] Z. Su, H. Wu, H. Chen, H. Guo, X. Cheng, Y. Song, X. Chen, H. Zhang, *Nano Energy* 42 (2017) 129.
- [37] F. Peng, D. Liu, W. Zhao, G. Zheng, Y. Ji, K. Dai, L. Mi, D. Zhang, C. Liu, C. Shen, *Nano Energy* 65 (2019) 104068.
- [38] H. Wu, Z. Su, M. Shi, L. Miao, Y. Song, H. Chen, M. Han, H. Zhang, *Adv. Funct. Mater.* 28 (2018) 1704641.
- [39] H. Guo, H. Wu, Y. Song, L. Miao, X. Chen, H. Chen, Z. Su, M. Han, H. Zhang, *Nano Energy* 58 (2019) 121.
- [40] H. Guo, X. Chen, L. Miao, H. Wang, J. Wan, H. Zhang, *IEEE Transducers* (2019) 554.
- [41] W. Wu, X. Wen, Z.L. Wang, *Science* 340 (2013) 952.
- [42] L. Nela, J. Tang, Q. Cao, G. Tulevski, S.-J. Han, *Nano Lett.* 18 (2018) 2054.
- [43] S. Fu, J. Tao, W. Wu, J. Sun, F. Li, J. Li, Z. Huo, Z. Xia, R. Bao, C. Pan, *Adv. Mater. Technol.* 4 (2019) 1800703.
- [44] T. Yamada, Y. Hayamizu, Y. Yamamoto, Y. Yomogida, A. Izadi-Najafabadi, D. N. Futaba, K. Hata, *Nat. Nanotechnol.* 6 (2011) 296.
- [45] X. Chen, L. Miao, H. Guo, H. Chen, Y. Song, Z. Su, H. Zhang, *Appl. Phys. Lett.* 112 (2018) 203902.
- [46] K.-I. Jang, S.Y. Han, S. Xu, K.E. Mathewson, Y. Zhang, J.-W. Jeong, G.-T. Kim, R. C. Webb, J.W. Lee, T.J. Dawidczyk, R.H. Kim, Y.M. Song, W.-H. Yeo, S. Kim, H. Cheng, S.I. Rhee, J. Chung, B. Kim, H.U. Chung, D. Lee, Y. Yang, M. Cho, J. G. Gaspar, R. Carbonari, M. Fabina, G. Gratton, Y. Huang, J.A. Rogers, *Nat. Commun.* 5 (2014) 4779.
- [47] J. Yun, Y. Lim, G.N. Jang, D. Kim, S.-J. Lee, H. Park, S.Y. Hong, G. Lee, G. Zi, J. S. Ha, *Nano Energy* 19 (2016) 401.
- [48] S. Niu, N. Matsuhisa, L. Beker, J. Li, S. Wang, J. Wang, Y. Jiang, X. Yan, Y. Yun, W. Burnett, A.S.Y. Poon, J.B.-H. Tok, X. Chen, Z. Bao, *Nat. Electron.* 2 (2019) 361.



Haobin Wang received the B.S. degree from Jilin University, Changchun, in 2018. He is currently pursuing the Ph.D. degree at the National Key Laboratory of Nano/Micro Fabrication Technology, Peking University, Beijing, China. His research interests mainly include micro-supercapacitors and the integration of self-charging system with energy harvesting modules and functional sensors.



Yu Song received the B.S. degree in Electronic Science & Technology from Huazhong University of Science and Technology, China, in 2015. He is currently pursuing the Ph.D. degree at the National Key Laboratory of Nano/Micro Fabrication Technology, Peking University, Beijing, China. He majors in MEMS and his research is focusing on supercapacitors and self-charging power system.



Hang Guo received his B.S. degree from Huazhong University of Science and Technology (HUST) in 2017 and now is a Ph.D. student at Academy for Advanced Interdisciplinary Studies in Peking University. His research interests focus on electronic skin and self-powered nanosystems.



Ji Wan received his B.S. degree from School of Electronics Engineering and Computer Science, Peking University, Beijing, China. He is currently pursuing the Ph.D. degree at the National Key Laboratory of Nano/Micro Fabrication Technology, Peking University, Beijing, China. His research interests mainly include self-powered electronic skin and composite materials.



Liming Miao received the B.S. degree from Peking University, Beijing, in 2017. He is currently pursuing the Ph.D. degree at the National Key Laboratory of Nano/Micro Fabrication Technology, Peking University, Beijing, China. His research interests mainly include wrinkle structure and triboelectric nanogenerator.



Chen Xu received the B.S. degree from School of Information And Electronics, Beijing Institute of Technology, Beijing, China. Now he is a Ph.D. student at Academy for Advanced Interdisciplinary Studies in Peking University. His research interests mainly include triboelectric nanogenerator and self-powered nanosystems.



Xuexian Chen received the B.S. degree from the University of Electronic Science and Technology of China, Chengdu, in 2015. She is currently pursuing the Ph.D. degree at the National Key Laboratory of Nano/Micro Fabrication Technology, Peking University, Beijing, China. Her research interests mainly include design and fabrication of hybrid nanogenerator and electrospinning process.



Zhongyang Ren received the B.E. degree from FuZhou University, FuZhou, in 2017. And then he pursuing the M.E. degree at FuZhou University, and also as a joint student at the National Key Laboratory of Nano/Micro Fabrication Technology, Peking University, Beijing, China. His research interests mainly include optoelectronic materials and devices and the hybrid energy harvester.



Hai-Xia (Alice) Zhang (SM'10) received her Ph.D at Huazhong University of Sci.&Tech. at 1998, then finished her Post-Doc research in Tsinghua University and joined Peking University at 2001 as a faculty member, her research focus on micro/nano energy harvesting technology and smart system. She authored and co-authored 300 + peer reviewed scientific articles on the prestigious journals, edited and co-edited 9 books and book chapters, and held 42 patents including 3 US patents. She is very active in academic service, was the founder and general Chair of IEEE NEMS conference, NTC Beijing Chapter Chair. She serves on editorial board of IEEE Tnano, JMEMS, Microsystem and Nanoengineering et al. She won National Invention Award of Science & Technology at 2006, Geneva Invention Gold Medal at 2014.